Synthesis, Structure, and Characterization of the Hexagonal Provskite $Ba_5In_{0.93}Mn_4O_{14.40}$

Congling Yin,[†] Guobao Li,*[,†] Tounan Jin,[‡] Liping You,[§] Julian Tao,[△] James W. Richardson,[△] Chun-K. Loong,[△] Junliang Sun,[†] Fuhui Liao,[†] and Jianhua Lin*[,†]

Beijing National Laboratory for Molecular Sciences, State Key Laboratory of Rare Earth Materials Chemistry and Applications, College of Chemistry and Molecular Engineering, and Electron Microscopy Laboratory, Peking University, Beijing 100871, P.R. China, College of Material Science and Engineering, Beijing University of Technology, Beijing 100022, P.R. China, and Intense Pulse Neutron Source Division, Argonne National Laboratory, Argonne, Illinois 60439

Received September 4, 2007. Revised Manuscript Received December 16, 2007

$Ba_5In_{0.93}Mn_4O_{14.40}$ was synthesized in air at 1300 °C by traditional solid state reaction and structurally characterized using powder X-ray diffraction, neutron diffraction, and selected area electron diffraction (SAED). It crystallizes in the hexagonal space group $P6_3/mmc$ with $a = 5.7389(1)$ Å and $c = 23.6418(1)$ Å and was formed by pseudoclose-packed BaO_{3-x} layers in a sequence of $(cchhh)_2$ with In and Mn cations occupying the oxygen octahedral holes.

Introduction

Recently, considerable interest has been focused on doped $BaMnO_3$ compounds with hexagonal perovskite related structures, because of their variant structures and relative high dielectric permittivity.[1–4] Several systems including $BaTi_xMn_{1-x}O_3$,[1] $BaCa_xMn_{1-x}O_{3-\delta}$,[2,3] $BaIr_xMn_{1-x}O_3$,[4] $BaLn_xMn_{1-x}O_{3-\delta}$ (Ln = rare earth element),[5–7] $BaIn_xMn_{1-x}O_{3-\delta}$,[8] $BaCo_xMn_{1-x}O_{3-\delta}$,[9–11] and $BaFe_xMn_{1-x}O_{3-\delta}$[12–14] have been reported. For these hexagonal perovskite related systems with the formula $ABO_{3-\delta}$, the structures can be constructed by pseudoclose-packed AO_{3-x} layers (some oxygen vacancies are randomly present in the close-packed AO_3 layers), with the B cations occupying octahedral sites. Further, in some case ordered oxygen vacancies are present in certain AO_{3-x} layers. In $BaCa_xMn_{1-x}O_{3-\delta}$,[2,3] for example, oxygen deficient layer, $AO_2\square_O$ ($\square_O$ represents the oxygen deficiency), appears in the structure (see Figure 1, shown as the c′ layer), which results in the alternative stacking of the octahedral BO_6 and tetrahedral BO_4 layers. As a general expression, the AO_{3-x} layers in the perovskite related structures can be considered as either a cubic layer (c) or a hexagonal layer (h) depending on the neighboring layers (cubic layer, A**B**C; hexagonal layer, A**B**A). Including possible oxygen deficient layers ($AO_2\square_O$), we may also have deficient a cubic layer (c′) and deficient hexagonal layer (h′). Stacking of these quasi-close-packing layers may lead to enormous structure types. Figure 1 shows a few examples, where one can see that the different structure types are generated through appropriate stacking of these quasi-close-packing layers for the doped $BaMnO_3$ compounds.

In addition to the structure diversity, some of the doped $BaMnO_3$ compounds exhibit high dielectric permittivity. For instance, the dielectric property of 12R $Ba_4YMn_3O_{11.5}$,[7] a doped $BaMnO_3$ compound with a $(cchh)_3$ stacking sequence, is comparable to that of $CaCu_3Ti_4O_{12}$ (CCTO),[15–19] a well-known compound showing high dielectric permittivity. The high dielectric permittivity of CCTO was attributed mainly

* Corresponding authors. E-mail: liguobao@pku.edu.cn (G.L.) and jhlin@pku.edu.cn (J.L.). Tel.: (8610)62750342. Fax: (8610)62753541.
† Beijing National Laboratory for Molecular Sciences, Peking University.
‡ Beijing University of Technology.
§ Electron Microscopy Laboratory, Peking University.
△ Argonne National Laboratory.

(1) Keith, G. M.; Kirk, C. A.; Sarma, K.; Alford, N. M.; Cussen, E. J.; Rosseinsky, M. J.; Sinclair, D. C. *Chem. Mater.* **2004**, *16*, 2007–2015.
(2) Floros, N.; Michel, C.; Hervieu, M.; Raveau, B. *Chem. Mater.* **2000**, *12*, 3197–3201.
(3) Floros, N.; Michel, C.; Hervieu, M.; Raveau, B. *J. Solid State Chem.* **2002**, *168*, 11–17.
(4) Jordan, N. A.; Battle, P. D. *J. Mater. Chem.* **2003**, *13*, 2220–2226.
(5) Fuentes, A. F.; Boulahya, K.; Amador, U. *J. Solid State Chem.* **2004**, *177*, 714–720.
(6) Rabbow, C.; Mueller-Buschbaum, H. K. *Z. Naturforsch.* **1994**, *49B*, 1277–1281.
(7) Kuang, X. J.; Bridges, C.; Allix, M.; Claridge, J. B.; Hughes, H.; Rosseinsky, M. J. *Chem. Mater.* **2006**, *18*, 5130–5136.
(8) Créon, N.; Michel, C.; Hervieu, M.; Maignan, A.; Raveau, B. *Solid State Sci.* **2003**, *5*, 243–248.
(9) Miranda, L.; Ramírez-Castellanos, J.; Varela, A.; González-Calbet, J.; Parras, M.; Hernando, M.; Fernández-Díaz, M. T. *Chem. Mater.* **2007**, *19*, 1503–1508.
(10) Gibb, T. C. *J. Mater. Chem.* **1992**, *2*, 387–393.
(11) Taguchi, H.; Shimada, M.; Kanamaru, F.; Koizumi, M.; Takeda, Y. *J. Solid State Chem.* **1976**, *18*, 299–302.
(12) Caignaert, V.; Hervieu, M.; Domenges, B.; Nguyen, N.; Pannetier, J.; Raveau, B. *J. Solid State Chem.* **1988**, *73*, 107–117.
(13) Miranda, L.; Ramírez-Castellanos, J.; Hernando, M.; Varela, A.; González-Calbet, J. M.; Parras, M. *Eur. J. Inorg. Chem.* **2007**, 2129–2135.
(14) Miranda, L.; Boulahya, K.; Varela, A.; González-Calbet, J. M.; Parras, M.; Hernando, M.; Fernández-Díaz, M. T.; Feteira, A.; Sinclair, D. C. *Chem. Mater.* **2007**, *19*, 1503–1508.
(15) Subramanian, M. A.; Li, D.; Duan, N.; Reisner, B. A.; Sleight, A. W. *J. Solid State Chem.* **2000**, *151*, 323–325.
(16) Ramirez, A. P.; Subramanian, M. A.; Gardel, M.; Blumberg, G.; Li, D.; Vogt, T.; Shapiro, S. M. *Solid State Commun.* **2000**, *115*, 217–220.
(17) Homes, C. C.; Vogt, T.; Shapiro, S. M.; Wakimoto, S.; Ramirez, A. P. *Science* **2001**, *293*, 673–676.
(18) Sinclair, D. C.; Adams, T. B.; Morrison, F. D.; West, A. R. *Appl. Phys. Lett.* **2002**, *80*, 2153–2155.
(19) Adams, T. B.; Sinclair, D. C.; West, A. R. *Adv. Mater.* **2002**, *14*, 1321–1323.

10.1021/cm7025152 CCC: $40.75
Published on Web 02/20/2008

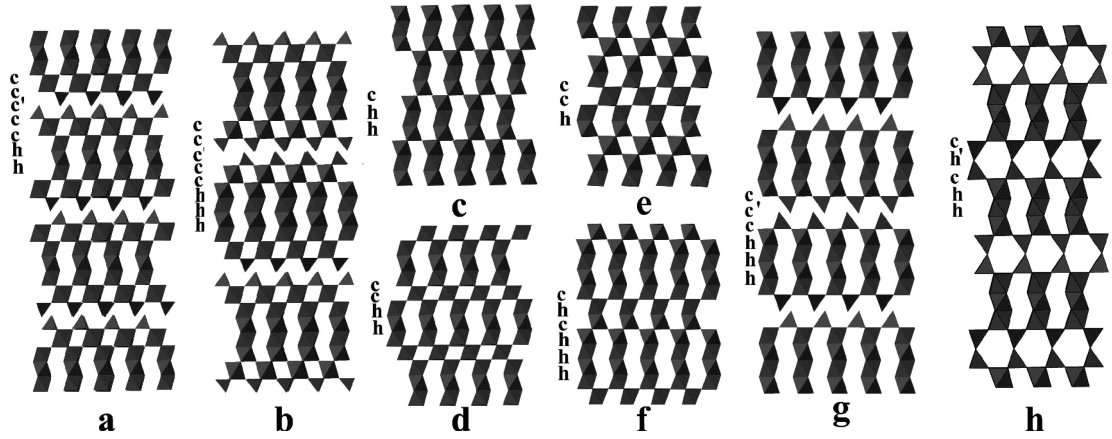

Figure 1. Stacking sequences for the main reported doped $BaMnO_3$ compounds with hexagonal structure. (a) 21R $Ba_7Ca_2Mn_5O_{20}$,[3] (b) 16H $Ba_4Ca_{0.9}Mn_{3.1}O_{11.3}$,[2] (c) 9R $BaIr_xMn_{1-x}O_3$,[4] (d) 12R $Ba_4CeMn_3O_{12}$,[5] (e) 6L $Ba_3ErMn_2O_9$,[6] (f) 6H $BaFe_{0.233}Mn_{0.767}O_{2.87}$,[12] (g) 12H $BaCo_{0.60}Mn_{0.40}O_{2.83}$,[9] and (h) 10H $BaMn_{0.4}Fe_{0.6}O_{2.73}$.[13]

to the internal barrier layer capacitance (IBLC) effect,[18,19] where the insulating grain boundaries block the migration of the charge carriers in the semiconductive grains. In the structure of 12R $Ba_4YMn_3O_{11.5}$ (Figure 1d), the face-sharing Mn_3O_{12} octahedral trimers are separated by YO_6 octahedral layers so that the structure itself may be regarded as a system containing IBLC, which induces the high relative dielectric permittivity. On the structural point of view, the main feature in the structures of the doped $BaMnO_3$ with hexagonal structure (see Figure 1) is that the MnO_6 octahedra are usually connected to chains by face sharing, and the chains are further separated by other chains or the MO_6 octehedra with corner sharing, which may be reagarded as a system containing IBLC. Therefore, we carried out systematic study on $BaM^{III}_xMn_{1-x}O_{3-\delta}$ (M^{III} = In, Bi, and rear earth elements) to search the high dielectric permittivity materials. Here, we report the synthesis, structure, and dielectric property of a new compound 10H $Ba_5In_{0.93}Mn_4O_{14.40}$ (**1**), which is isostructural to 10H $Cs_5Cd_{1.25}Ni_{3.75}F_{15}$[20] with the $(cchhh)_2$ stacking sequences of the AO_{3-x} layers.

Experimental Section

Compound **1** was synthesized via high temperature solid-state reaction. The starting materials $BaCO_3$ (A.R.), In_2O_3 (99.95%), and MnO_2 (A.R.) with the mole ratio of Ba:In:Mn = 5.000:0.945:4.000 were mixed in an agate mortar and pestle and heated in an alumina crucible at 1000 °C for 10 h. Then, the sample was reground, pressed into pellets (20 ton/cm^2), and heated at 1300 °C for 30 h with several intermediate pressing and grinding steps.

The phase purity of the sample was checked by powder X-ray diffraction on a Rigaku D/Max-2000 diffractometer with graphite monochromatized Cu Kα radiation at 40 kV, 100 mA. Data were collected in the range of 7–120° with step scanning mode for Rietveld refinement carried out with GSAS program.[21,22] The neutron diffraction data were collected at room temperature on the Special Environment Powder Diffractometer at the Intense Pulsed Neutron Source, Argonne National Laboratory. Selected area electron diffraction (SAED), convergent-beam electron diffraction (CBED), and high-resolution electron microscopy (HREM) were carried out on Tecnai G^2 F30 with an accelerating voltage of 300 KV. The magnetic properties were investigated with a Quantum Design MPMS-SS superconducting quantum interference device (SQUID) magnetometer from 2 to 300 K and a vibrating sample magnetometer from 300 to 750 K. The temperature dependence of magnetic susceptibilities was measured under a 1000 Oe external field. Corrections have been applied for the core diamagnetic susceptibility and the sample holder. The X-ray photoelectron spectroscopy (XPS) patterns were acquired with a UK Kratos Axis Ultra spectrometer with Al Kα X-ray source operated at 15 kV, 15 mA. The chamber pressure was less than 5.0×10^{-9} Torr. Electron binding energies were calibrated against the C 1s emission at E_b = 284.8 eV. The Ba content of **1** was determined by $BaSO_4$ gravimetry, and the quantities of In and Mn were determined by complexometric titration with the titrant of ethylenediaminetetraacetic acid (EDTA; see Supporting Information for the details). An average oxidation state of 4.01(4) for Mn was determined by an iodometric titration method.[23] The Mn(IV) in this compound was confirmed by the XPS data (see Figure S2 in the Supporting Information), which shows the binding energy is about 641.8 eV ($2p_{3/2}$) for **1**, comparable to 642.1 eV for MnO_2.[24] Hydrogen-reduction thermogravimetry was used to determine the oxygen content of **1**. A small sample of powder (about 20 mg) was placed in an alumina crucible in a Netzsch STA 449C thermogravimetric analyzer and heated at 10 °C min^{-1} in a flowing 60% H_2/40% Ar atmosphere from room temperature to 800 °C.

AC impedance was measured with a HP4192A impedance analyzer with ac voltage of 100 mV and frequency range of 5 Hz to 12 MHz between 40 and 400 °C. The density of the pellet estimated using the Archimedean method is about 75% of the ideal density. The electrode was painted with Pt paste on faces of the pellet and then treated at 800 °C for 30 min. The impedance data analysis and equivalent circuit fitting were carried out with EQUIVCRT software.[25] The microstructure of the $Ba_5In_{0.93}Mn_4O_{14.40}$ ceramic samples was examined using a Quanta 200F scanning electron microscope, and the energy dispersive analysis by X-ray (EDAX) was used to examine the compositions.

(20) Dance, J. M.; Darriet, J.; Tressaud, A.; Hagenmuller, P. *Z. Anorg. Allg. Chem.* **1984**, *508*, 93–99.
(21) Rietveld, H. M. *J. Appl. Crystallogr.* **1969**, *2*, 65–71.
(22) Larson, A. C.; Von Dreele, R. B. *General Structure Analysis System (GSAS)*, Los Alamos National Laboratory Report LAUR 86-748; Los Alamos, NM, 2004.
(23) Jeffery, G. H., Bassett, J., Mendham, J., Denney, R. C., Eds. *Vogel's Textbook of Quantitative Chemical Analysis*, 5th ed.; Longman Scientific & Technical: Harlow, Essex, U.K., 1989.
(24) Moulder, J. F.; Stickle, W. F.; Sobol, P. E.; Bomben, K. D. In *Handbook of X-ray Photoelectron Spectroscopy*, 2nd ed.; Chastain, J., King, R. C., Jr., Eds.; Physical Electronics, Inc.: Eden Prairie, 1995.
(25) Boukamp, B. A. *Solid State Ionics* **1986**, *20*, 31–44.

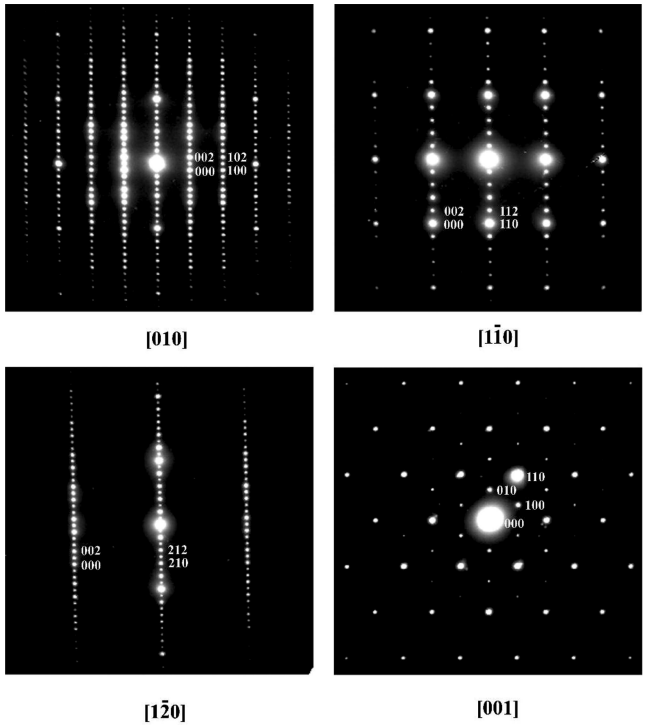

Figure 2. SAED patterns of **1**.

Structure Determination. The structure was determined by using *ab initio* method on powder X-ray diffraction data. The powder diffraction data can be indexed[26] to a hexagonal cell with $a = 5.7389$ Å and $c = 23.6418$ Å. The systematic absence of the reflections indicated the possible space groups, $P6_3/mmc$, $P\bar{6}2c$, $P6_3mc$, $P\bar{3}1c$, or $P31c$. Figure 2 shows SAED patterns in [010], [1$\bar{1}$0], [1$\bar{2}$0], and [001] zones, which confirm the primary hexagonal lattice and the systematic absence of the reflections $hh\bar{2}hl$: $l = 2n + 1$. To further determine the space groups, second-harmonic generation (SHG) coefficient measurement was conducted on powder samples by using the Kurtz−Perry method[27] with a YAG: Nd^{3+} laser (1064 nm). Compound **1** does not show second order nonlinear optical effect. Therefore, although we cannot exclude the central asymmetric space groups, the central symmetric space groups, $P6_3/mmc$ or $P\bar{3}1c$, are highly preferred. In addition, the piezoelectric coefficient (d_{33}) is not detectable for a ceramic sample, which also supports that the possible space group is either $P6_3/mmc$ or $P\bar{3}1c$. The symmetry of the 6-fold axis can be found in the CBED taken along [001] shown in Figure 3. Therefore, the space group for **1** is chosen as $P6_3/mmc$.

The structure solution was established in the space group $P6_3/mmc$ by using the direct method,[28] where barium, indium, manganese, and part of the oxygen positions can be directly located. The rest of the oxygen positions were obtained by subsequent difference Fourier analysis.[29] The final structure refinement was carried out simultaneously on powder X-ray diffraction data and neutron diffraction data using the Rietveld method with isotropic displacement parameters for all atoms. The fitting is very good as shown in Figure 4 for the neutron diffraction data (and Figure S3 for the X-ray diffraction data in Supporting Information). The refined atomic parameters and isotropic displacement parameters are listed in Table 1, and the selected bond lengths are listed in Table 2. Initially, Mn and In were randomly distributed over the three available crystallographic positions (see Table 1) in a 0.93/4 ratio according to the $Ba_5In_{0.93}Mn_4O_{14.40}$ formula. Subsequent

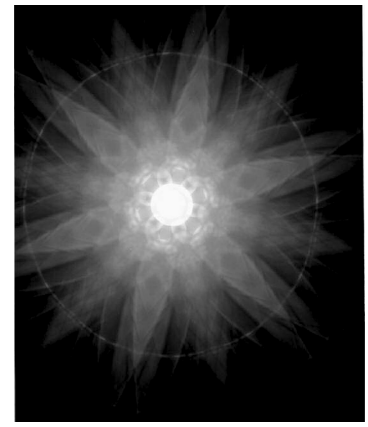

Figure 3. CBED patterns of **1** taken along the [001] direction.

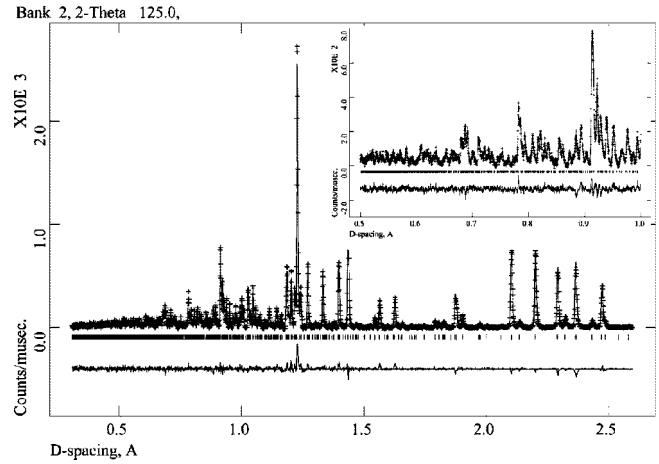

Figure 4. Rietveld plots of the powder neutron diffraction pattern for **1** in space group $P6_3/mmc$.

Table 1. Rietveld Refinement Details and BVS Values of Compound 1 in the Space Group $P6_3/mmc$[a]

atom	site	*x*, *y*, *z*	U_{equiv}	occupy
Ba1	2d	2/3, 1/3, 1/4	0.0082(1)	1
Ba2	4f	2/3, 1/3, 0.4444(1)	*b*−*d*	1
Ba3	4e	0, 0, 0.3458(1)	0.0052(1)	1
In1	2a	0, 0, 1/2	*b*−*d*	0.943(1)
Mn1	4f	1/3, 2/3, 0.4066(1)	0.0026(1)	1
Mn2	4f	1/3, 2/3, 0.3011(1)	0.0045(1)	1
O1	6h	0.1830(1), 0.8170(1), 1/4	0.0017(1)	1
O2	12k	0.1747(1),0.3493(1), 0.4485(1)	*b*−*d*	0.903(1)
O3	12k	0.4814(1), 0.9628(1), 0.3518(1)	0.0036(1)	1

$R^X_P = 0.060$, $R^X_{wp} = 0.082$, $R^X_F{}^2 = 0.044$; $R^N_P = 0.047$, $R^N_{wp} = 0.059$, $R^N_F{}^2 = 0.107$; $\chi^2 = 3.06$[e]

[a] The corresponding lattice parameters are $a = 5.7389(1)$ Å, $c = 23.6418(1)$ Å. [b−d] Anisotropic temperature factors for (a) Ba2, $U_{11} = 0.0032(1)$, $U_{22} = 0.0032(1)$, $U_{33} = 0.0085(1)$, $U_{12} = 0.0016(1)$, $U_{13} = 0$, $U_{23} = 0$; (b)In1, $U_{11} = 0.0038(1)$, $U_{22} = 0.0038$, $U_{33} = 0.0076(1)$, $U_{12} = 0.0019(1)$, $U_{13} = 0$, $U_{23} = 0$; (c)O2, $U_{11} = 0.0039(1)$, $U_{22} = 0.0020(1)$, $U_{33} = 0.0043(1)$, $U_{12} = 0.0014(1)$, $U_{13} = 0.0006(1)$, and $U_{23} = 0.0012(1)$. [e] R^X_P, R^X_{wp} and $R^X_F{}^2$ are R factors for X-ray diffraction data, and R^N_P, R^N_{wp} and $R^N_F{}^2$ for neutron diffraction data.

(26) Dong, C. *J. Appl. Crystallogr.* **1999**, *32*, 838.
(27) Kurtz, S. K.; Perry, T. T. *J. Appl. Phys.* **1968**, *39*, 3798–3813.
(28) Altomare, A.; Burla, M. C.; Cascarano, G.; Giacovazzo, C.; Guagliardi, A.; Moliterni, A. G. G.; Polidiori, G. *J. Appl. Crystallogr.* **1995**, *28*, 842–846.
(29) Altomare, A.; Cascarana, G.; Giacovazzo, C.; Guagliardi, A. *SIRPOW user's manual*, 1992; Inst. di Ric. per lo Sviluppo di Metodologie Cristallografiche, CNR, c/o Dipartimento Geomineralogico, Campus Universitario, 70124 Bari, Italy.

Table 2. Selected Bonds in 1

bond length (Å)		bond length (Å)		bond length (Å)	
Ba1−O1 × 6	2.874(1)	Ba3−O1 × 3	2.905(1)	Mn1−O3 × 3	1.959(1)
Ba1−O3 × 6	3.031(1)	Ba3−O2 × 3	2.985(1)	Mn2−O1 × 3	1.922(1)
Ba2−O2 × 6	2.872(1)	Ba3−O3 × 6	2.879(1)	Mn2−O3 × 3	1.898(1)
Ba2−O2 × 3	2.982(1)	In1−O2 × 6	2.120(1)		
Ba2−O3 × 3	2.860(1)	Mn1−O2 × 3	1.863(1)		

refinement showed that the In1 sites are almost occupied by indium (∼94%) and the Mn1 and Mn2 sites are occupied by manganese (∼100%). Finally, a value of 0.943 was obtained for the site of In by refinement when the sites of Ba and Mn are fully occupied, which agrees well with the quantitative analysis result of the ratio 5.05:0.93:4.00 for Ba:In:Mn. In addition, the occupations of the site of O1 and O3 were very near 1 and set to 1, but the occupation of the site of O2 was far from 1 and finally was refined as 0.903 with the consideration that the all Mn atoms are Mn(IV). Combining with the result from the hydrogen-reduction thermogravimetry (see Supporting Information), the formula of **1** was noted as $Ba_5In_{0.93}Mn_4O_{14.40}$ because the result from quantitative analysis is more believable. The presence of anionic vacancies may generate BaO_{3-y} layers that are no longer close-packed, making the atomic displacement through the layer easier;[9] however, the presence of indium vacancies may induce the atomic displacement perpendicular to the layer easier. For this reason, the anisotropic displacement parameters for Ba2, In1, and O2 have been considered; the obtained values reflect a relative large delocalization along the *z*-axis.

Results and Discussion

How to Find $Ba_5In_{0.93}Mn_4O_{14.40}$. At the beginning, a series of samples with the nominal formula of $Ba_5In_{1-x}Mn_{4+y}O_{15-\delta}$ ($x = 0, 0.01, 0.015, 0.025, 0.035, 0.045, 0.055, 0.065, 0.08$; $y = 0, \pm0.02, \pm0.04, \pm0.06, \pm0.08$) were synthesized via high temperature solid-state reaction to try the supposed compound $Ba_5InMn_4O_{14.5}$ containing the expected cchhh stacking sequence after knowing the compound 12R $Ba_4InMn_3O_{11.5}$[8] with a $(cchh)_3$ stacking sequence. A pure phase was obtained for the sample with the nominal formula of $Ba_5In_{0.945}Mn_4O_{15-\delta}$, which turned out to be $Ba_5In_{0.93}Mn_4O_{14.40}$ as mentioned above;the others contain the impurity (see Supporting Information for the details).

Structure Description. Structural refinement reveals that the O vacancies are located in a disordered manner solely at the O2 site (Figure 5 and Table 1) within the two c-BaO_{3-x} layers. This results in a coordinated number of less than 6 for a significant fraction of the In and Mn1 species. The mean Mn1 coordination number of 5.71(1) means that 29% of the Mn1 sites at the edges of the tetramers are five-coordinate. This is an unusual coordination number for Mn^{4+}, although a similar situation has been observed in 12R $Ba_4YMn_3O_{11.5}$[7] and $Ba_4InMn_3O_{11.5}$.[8] The mean In coordination number of 5.42(1) corresponds to 58% of In^{3+} cations being five coordinate. This situation is quite compatible with the ability of In^{3+} to exhibit the 5-fold coordination.[35]

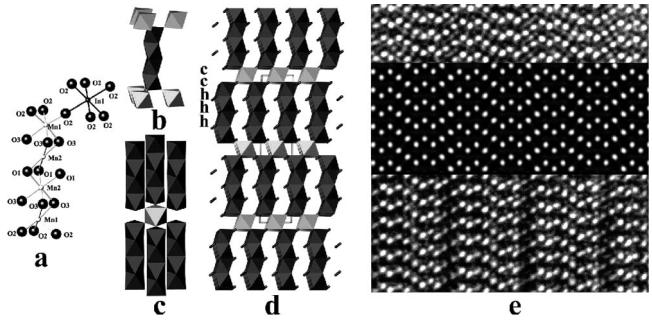

Figure 5. Structure descriptions of $Ba_5In_{0.93}Mn_4O_{14.40}$: (a) the coordination geometries of In and Mn, (b) a view of six InO_6 octahedra linking to a Mn_4O_{15} tetramer, (c) a view of six Mn_4O_{15} tetramers linking to an InO_6 octahedra, (d) a projection of the structure along the *a*-axis, (e) the HRTEM image of $Ba_5In_{0.93}Mn_4O_{14.40}$ in the [010] zone; the simulated image has been calculated for the positional parameters listed in Table 1, focus value –70 nm and crystal thickness 28 nm.

To simplify the description of the structure of **1**, the randomly scattered O vacancies at the O2 site were noted as $\square_O$ and were treated as pseudo-oxygen in mind. In this case, "InO_6" (or "MnO_6") octahedron is talked about, which may include $InO_5\square_O$ (or $MnO_5\square_O$) octahedron. Similarly, considering the randomly scattered In vacancies (noted as $\square_{In}$) at the In1 site, some "InO_6" octahedra may be $\square_{In}O_6$ or $\square_{In}O_5\square_O$ octahedra. Keeping these in mind, the structure of **1** was illustrated in Figure 5. In the structure of **1**, In occupies the 2a site (0, 0, 0) in $\bar{3}m$ symmetry and forms an octahedron with oxygen atoms (or oxygen vacancies) that shares corners with six neighboring "MnO_6" octahedra (see Figure 5c). The In−O bond is regular (2.120(1) Å). The two Mn sites are all at 4f (1/3, 2/3, *z*) in a local symmetry of 3*m*. The "MnO_6" octahedra share faces forming "Mn_4O_{15}" (Mn_4O_{15} or $Mn_4O_{14}\square_O$, or $Mn_4O_{13}(\square_O)_2$) tetramer as shown in Figure 5a, which further connected with six "InO_6" octahedra as shown in Figure 5b. The overall structure, in fact, can be considered as a typical intergrowth of the cubic perovskite and hexagonal perovskite, that is, a cubic perovskite layer ("InO_6") and four hexagonal perovskite layers alternate along the *c*-axis (Figure 5d). The intergrowth of the hexagonal and cubic perovskite layers can be clearly visualized in HRTEM image of $Ba_5In_{0.93}Mn_4O_{14.40}$ in the [010] zone (Figure 5e), which is simulated very well with the reported structure. Alternatively, the structure of **1** can also be described from the pseudoclose-packed AO_{3-x} layers with a stacking sequence of $(cchhh)_2$ along the *c*-axis, and the Mn and In ions occupy the octahedral sites. Ba atoms, on the other hand, are located in a 12-coordinated polyhedron with oxygen atoms or oxygen vacancies. As we know, the possible stacking sequences of the 10H perovskite related materials with double five-layers are just $(ccccch)_2$, $(ccchh)_2$, $(cchhh)_2$, $(chchh)_2$, and $(hhhhh)_2$ (for simplicity, here c includes c′ and

(30) Battle, P. D.; Davison, C. M.; Gibb, T. C.; Vente, J. F. *J. Mater. Chem.* **1996**, *6*, 1187–1190.
(31) Kuang, X.; Allix, M. M. B.; Claridge, J. B.; Niu, H. J.; Rosseinsky, M. J.; Ibberson, R. M.; Iddles, D. M. *J. Mater. Chem.* **2006**, *16*, 1038–1045.
(32) Adkin, J. J.; Hayward, M. A. *Chem. Mater.* **2007**, *19*, 755–762.
(33) Negas, T.; Roth, R. S. *J. Solid State Chem.* **1971**, *3*, 323–339.
(34) Hong, S. T.; Sleight, A. W. J. *Solid State Chem* **1997**, *132*, 407–410.
(35) Pistorius, C. W. F. T.; Kruger, G. J. *J. Inorg. Nucl. Chem.* **1976**, *38*, 1471–1475.

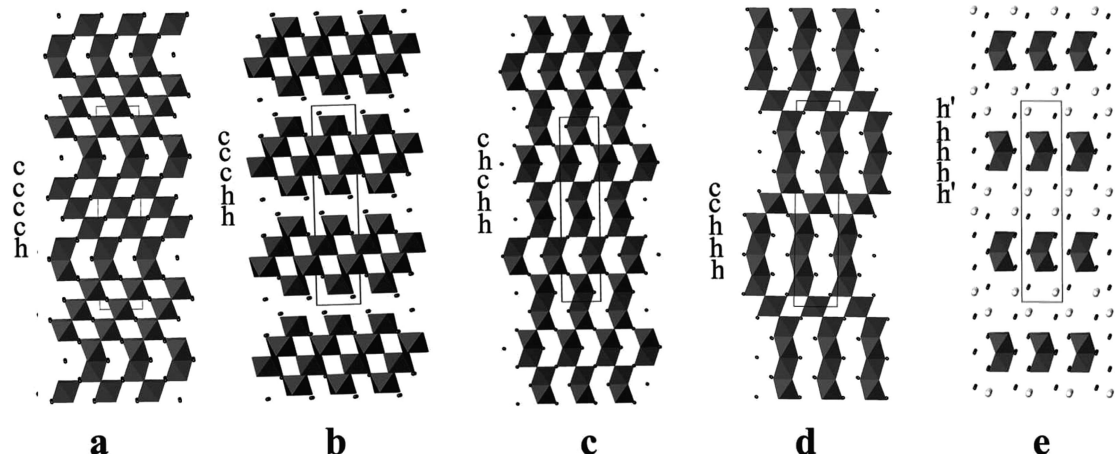

Figure 6. Reported stacking sequences of the 10H perovskite related materials with double five layers. (a)10H-$SrFe_{0.276}Mn_{0.724}O_{2.868}$,[30] (b)10H-$La_5Zn_{0.5}Ti_{3.5}O_{15}$,[31] (c) 10H-$BaMnO_{2.91}$[32] (or 10H-$BaMnO_{2.81}$[33]), (d) 10H-$Cs_5Cd_{1.25}Ni_{3.75}F_{15}$,[20] and (e) 10H-$Ba_5Ru_{1.6}W_{0.4}Cl_2O_9$.[34]

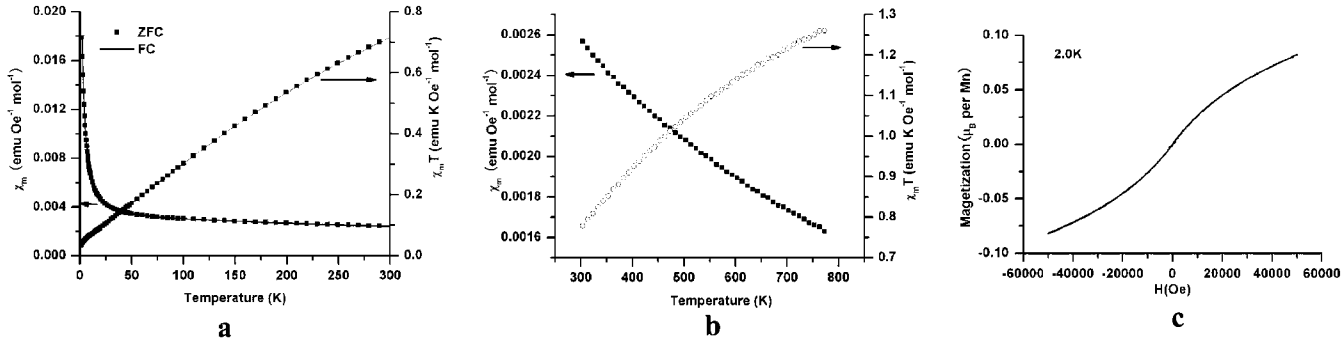

Figure 7. Magnetization data per molar Mn for **1**. (a) Zero-field-cooled and field-cooled data collected from 2 K to 300 K, (b) zero-filed-cooled data collected from 300 K to 750 K, and (c) the data collected as a function of field at 2.0 K.

h includes h′. That is, cccch may be c′ccch or c′c′cch and so on.). Four of them have been reported as presented in Figure 6 for complex oxides, but the sequence $(cchhh)_2$ for **1** has not been reported for oxide compounds although an example of $Cs_5Cd_{1.25}Ni_{3.75}F_{15}$[20] was reported.

There is another ternary phase, 12R $Ba_4InMn_3O_{11.5}$ (**2**), with a $(cchh)_3$ stacking sequence in the Ba−In−Mn−O system.[8] Although the compounds **1** and **2** crystallized in a different space group, $P6_3/mmc$ and $R\bar{3}m$, respectively, they have the similar values of the lattice parameter *a* (5.7389 Å for **1** and 5.7382 Å for **2**) and the average thickness of one layer (2.364 Å for **1** and 2.353 Å for **2**). In addition, for both compounds, they have very similar bond lengths for In−O (2.12Å for **1** and 2.17 Å for **2**) and Mn−O (1.86–1.96 Å for **1** and 1.83–1.92 Å for **2**).

Magnetic Property. The temperature dependence of the magnetic susceptibility of **1** measured in a field of 1000 Oe is shown in Figure 7. The two data sets were measured respectively with a SQUID (2–300 K) and a vibrating sample magnetometer (300–750 K). As shown in Figure 7a, there was no difference between the data collected under zero-field-cooled (ZFC) and field-cooled (FC) from 2 to 300K. No high temperature plateau in χ_mT(T) was present up to 800K (see Figure 7b). The χ_mT value decreased monotonously from 800K to 2K. No loop was found in M-H curve at 2K (see Figure 7c). These suggest that strong antiferromagnetic interactions are present within the face-sharing tetramers. Temperatures above 800K will be required to access the Curie–Weiss region in **1**. Different from other similar compound such as $Ba_4YMn_3O_{11.5}$,[7] no magnetic ordering was occurring down to 2 K for **1**, which indicated that the diamagnetic In^{3+} ion is a stronger hinter than Y^{3+} to hider the development of long-range correlations between the face-sharing octahedral units, resulting in the absence of clear signatures of magnetic order down to low temperatures.[7]

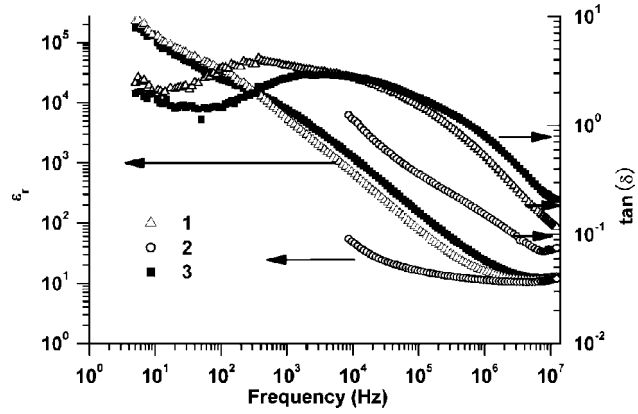

Figure 8. Frequency dependence of ε_r and tan δ values for **1** as obtained in air (1), annealing at 800 °C in flowing argon (2), and reannealing at 800 °C in flowing oxygen (3).

Dielectric Properties and Conductivity. Figure 8 shows frequency dependence of dielectric permittivity ε_r and the dielectric loss tan δ measured at 40 °C for the ceramic samples of **1** obtained in air, annealing at 800 °C in Ar for 12 h, and

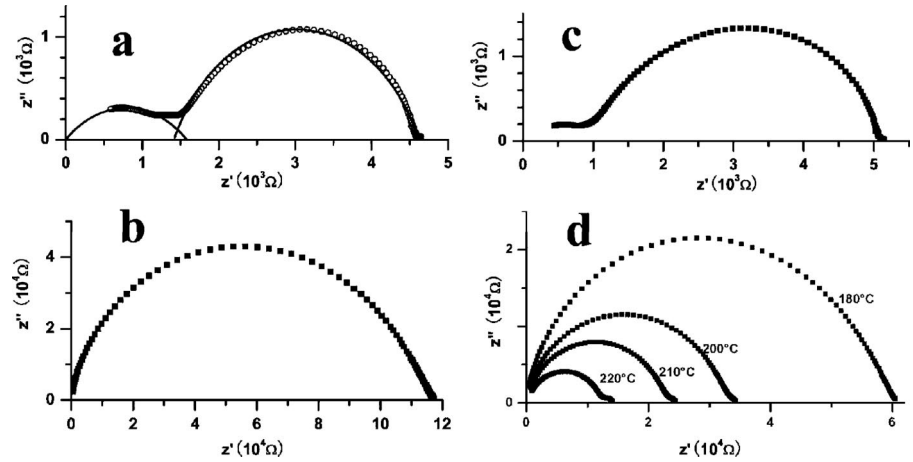

Figure 9. Complex impedance plots $Z''-Z'$ for **1** measured under different conditions: (a) measured at 150 °C in air for the pellet as obtained, (b) at 150 °C in O_2 atmosphere for the pellet annealed in Ar atmosphere at 800 °C for 12 h, (c) at 150 °C in O_2 atmosphere for the pellet reannealed at 800 °C for 12 h in O_2 atmosphere, and (d) in O_2 atmosphere for the pellet annealed in Ar atmosphere at 800 °C for 12 h.

reannealing at 800 °C in O_2 (after annealing at 800 °C in Ar for 12 h) for 12 h. The ε_r values depend strongly on the frequency; they are quite high (about 10^5) at low frequency but drop quickly (to about 10^1) at high frequency. Such behavior is different from that of $Ba_4YMn_3O_{11.5}$.[7] The atmosphere of the heating treatment shows strong influence to the dielectric permittivity. As shown in Figure 8, the samples obtained in air and reannealed in O_2 at 800 °C show a similar behavior, while the ε_r value of the sample annealed in Ar is significantly low. A similar result was also observed for the dielectric loss (tan δ); that is, the dielectric loss shows a similar behavior for the samples treated in air and O_2, while significant low dielectric losses were observed for the sample treated in Ar. The tan δ values are frequency-dependent and lower than that reported for $Ba_4YMn_3O_{11.5}$[7] in many frequency ranges. The dielectric permittivity ε_r increases when the temperature increases for the above three conditions (see Supporting Information). However, there was no any observable change in X-ray diffraction patterns among the samples as obtained, annealed in argon, and reannealed in oxygen atmosphere; the difference of the hydrogen-reduction thermogravimetry among them was very small (see Supporting Information for the details).

To understand the above dielectric behavior, the complex impedance of **1** treated under different conditions was measured and analyzed. Typical complex impedance plots $Z''-Z'$ are shown in Figure 9. The plot shown in Figure 9a was measured at 150 °C in air for the sample as obtained. It could be modeled on an equivalent circuit consisting of two parallel RQ elements connected in series, one RQ element for the bulk, and the other for the grain boundary response (here R represents resistor and Q is the constant phase element (CPE))[24,36] each corresponding to a semicircular arc in the impedance complex plane plots. Then an equivalent circuit consisting of one parallel R_bQ_b element for the gains and one parallel R_gQ_g element for the grain boundary connected in series was used to model the spectra (see solid lines Figure 9a). The data shown in Figure 9b were measured in an O_2 atmosphere for the sample treated at 800 °C for 12 h in Ar atmosphere. It seemed to be one semicircle, which was just the overlap of two semicircles

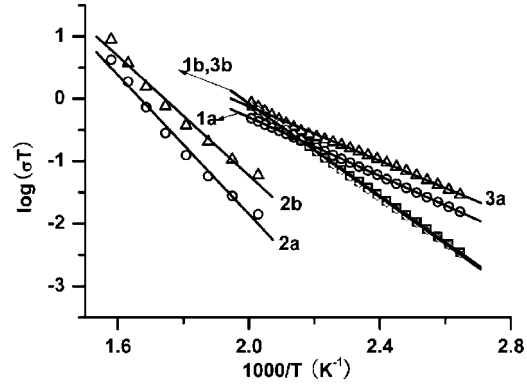

Figure 10. Temperature dependence of the conductivity of the grain (σ_b) and grain boundary (σ_g) for **1** under different conditions. 1a, σ_b measured in air for the pellet as obtained; 1b, σ_g measured in air for the pellet as obtained; 2a, σ_b measured in oxygen atmosphere for the pellet annealed under Ar atmosphere at 800 °C for 12 h; 2b, σ_g measured in oxygen atmosphere for the pellet annealed under Ar atmosphere at 800 °C for 12 h; 3a, σ_b measured in oxygen atmosphere for the pellet reannealed under oxygen atmosphere at 800 °C for 12 h; and 3b, σ_g measured in oxygen atmosphere for the pellet reannealed under oxygen atmosphere at 800 °C for 12 h.

confirmed by the high temperature data shown in Figure 9d. It is clear to see from Figure 9d that the semicircle for the grain boundary manifests itself when the temperature increases. At 220 °C, the two semicircles were clearly presented, which indicated that R_b (the resistance of the grain) was larger than R_g (the resistance of the grain boundary). The data also showed that the resistance of the grain became larger after annealing at 800 °C for 12 h in an Ar atmosphere. However, when the sample was reannealed at 800 °C for 12 h in O_2 atmosphere, the complex impedance plot $Z''-Z'$ was recovered to that for the sample as obtained (see Figure 9c).

The temperature dependent conductivity of the grain and grain boundary for the sample treated under different conditions can be calculated from the corresponding R_b and R_g, respectively, as shown in Figure 10. The conductivity agreed well with Arrhenius' law:

$$\sigma T = Ae^{-E_a/kT} \quad (1)$$

Here, T is the temperature in kelvin, σ the conductivity of the sample (Ω^{-1} cm^{-1}), A the pre-exponential factor, E_a the

(36) Irvine, J. T. S.; Sinclair, D. C.; West, A. R. *Adv. Mater.* **1990**, *2*, 132–138.

Table 3. Pre-Exponential Factor A and Activation Energy E_a for the Different Processes

conditions[a]	A^{b}[b]	E^{b}_{a}	A^{g}	E^{g}_{a}
1	2.6×10^4	0.47 eV	2.0×10^7	0.73 eV
2	2.0×10^9	1.11 eV	2.2×10^8	0.95 eV
3	1.8×10^4	0.43 eV	2.8×10^7	0.75 eV

[a] 1, the data obtained in air for the pellet as obtained; 2, in oxygen atmosphere for the pellet annealed under Ar atmosphere at 800 °C for 12 h; 3, in oxygen atmosphere for the pellet reannealed under O_2 atmosphere at 800 °C for 12 h. [b] A^{b} and E^{b}_{a}, the pre-exponential factor and the activation energy for the grain; A^{g} and E^{g}_{a}, for the grain boundary.

activation energy, and k the Boltzmann's constant. The corresponding values for the different pre-exponential factor A and the activation energy E_a are listed in Table 3.

The pre-exponential factor (it was positively related to the concentration of the charge carrier of the material) A^{g} for the grain boundary was larger than the factor A^{b} for the grain (see Table 3), indicating that more charge carriers appear in the grain boundary than in the grain. When the pellet was annealed at 800 °C under Ar atmosphere, much larger pre-exponential factors were found for both the grain and the grain boundary indicating that more charge carriers were created. And when the pellet was reannealed at 800 °C under oxygen atmosphere, the charge carriers were less and similar to the nonannealing sample as shown in Table 3. It was also understandable that when the pre-exponential factors were smaller, the concentration of the charge carriers was less, and then the transfer of the charge carries became easy to induce the smaller active energies as listed in Table 3.

In addition, as shown in Figure 10 and Table 3, the conductivity was very similar for the pellet as obtained measured in air and the pellet reannealed at 800 °C under oxygen atmosphere for 12 h measured in oxygen atmosphere. Below 180 °C, the grain was more conductive than the grain boundary. This may induce the high dielectric constant for this material by the internal barrier layer capacitance (IBLC) effect (see Supporting Information for the details). When the pellet was treated at 800 °C under Ar atmosphere for 12 h, its conductivity was lower and the grain boundary was more conductive than the grain, which lowered the dielectric constant of the material as shown in Figure 8 (see Supporting Information for the details).

Scanning electron microscopy (SEM) images of fractured sections revealed a porous microstructure (Figure 11a) for $Ba_5In_{0.93}Mn_4O_{14.40}$ pellets, as expected for the comparatively low density. The grain sizes were found to lie within the 1–5 μm range (Figure 11b). EDAX elemental analysis on different regions with an area of 20 μm^2 confirmed that the composition of the material was essentially homogeneous. No significant composition difference was found for the grain and grain boundary as shown by line scanning (see Supporting Information).

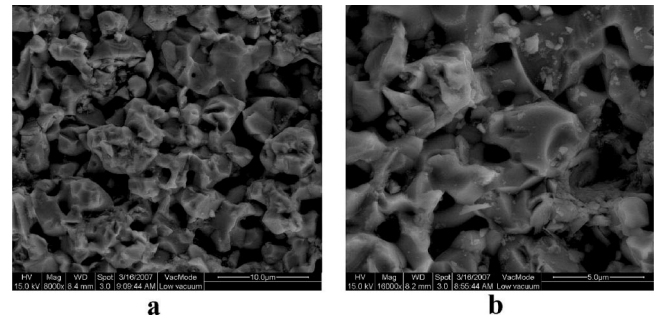

Figure 11. SEM images of fractured sections for $Ba_5In_{0.93}Mn_4O_{14.40}$ ceramic: (a) porous microstructure and (b) an enlarged area with clear grains and grain boundaries.

Conclusion

A new barium indium manganese oxide $Ba_5In_{0.93}Mn_4O_{14.40}$ has been synthesized at 1300 °C in air by traditional solid state reaction. It is a perovskite related compound, where the pseudoclose-packed BaO_{3-x} layers stack in the $(cchhh)_2$ sequences. Four "MnO_6" (including $MnO_5\square_O$) octahedra link to each other by face-sharing to form tetramers, which is linked by "InO_6" (including $InO_5\square_O$ or $\square_{In}O_5\square_O$) octahedra through corner-sharing. Strong antiferromagnetic interaction was found for $Ba_5In_{0.93}Mn_4O_{14.40}$, but no ordering is presented until 2 K. At room temperature, $Ba_5In_{0.93}Mn_4O_{14.40}$ shows high relative dielectric constant below 100 Hz with a large dielectric loss.

Acknowledgment. We thank the Dr. Guilin Wang (research and application of tunable all solid state laser of Key Laboratory of Optical Physics, Institute of Physics, Chinese Academy of Sciences) for the help with measuring the NLO effects of **1**. This work is supported by the National Natural Science Foundation of China (Grants 20471003 and 20531010).

Supporting Information Available: X-ray crystallographic file in CIF format; the details on the chemical analysis of **1**; calculated and observed X-ray diffraction pattern for **1**; the XPS spectrum of Mn 2p in **1**; typical powder X-ray diffraction patterns for the samples around **1**; comparison of X-ray diffraction patterns and hydrogen-reduction TG curves of the samples as obtained in air, annealed in argon, and reannealed in oxygen atmosphere; temperature dependence of ε_r for **1** treated at different conditions; comments on the internal barrier layer capacitance (IBLC) effect; the EDAX results for **1**; and calculated and observed X-ray diffraction pattern for $Ba_5SnMn_4O_{15}$ and $Ba_5Sb_{1-x}Mn_{4+x}O_{15}$ (PDF). This material is available free of charge via the Internet at http://pubs.acs.org.

CM7025152